Tracking metal evolution in arc magmas: Insights from the active volcano of La Fossa, Italy

Simone Costa, Paolo Fulignati, Anna Gioncada, Marco Pistolesi, Delphine Bosch, Olivier Bruguier

Tracking metal evolution in arc magmas: Insights from the active volcano of La Fossa, Italy

Simone Costa [a,b], Paolo Fulignati [b,*], Anna Gioncada [b], Marco Pistolesi [b], Delphine Bosch [c], Olivier Bruguier [c]

[a] Dipartimento di Scienze della Terra, Università di Firenze, via La Pira, 4, 50121 Firenze, Italy
[b] Dipartimento di Scienze della Terra, Università di Pisa, via S. Maria, 53, 56126 Pisa, Italy
[c] Géosciences Montpellier, Université de Montpellier, CNRS, Place E. Bataillon, 34095 Montpellier, France

A B S T R A C T

The mineralization potential of arc magmas depends, among other factors, on the timing of sulfide melt saturation relative to magma differentiation and to exsolution of a magmatic fluid phase. In fossil mineralized or barren systems, understanding the evolution of metals along the magma differentiation path is often hindered by late magmatic processes and hydrothermal alteration. To better understand the process of metal evolution "caught in the act" in crustal reservoirs, we analyzed magmatic sulfides and melt inclusions found within eruptive products from the active arc volcano, La Fossa (Vulcano Island, Italy), for the basalt to rhyolite compositional spectrum. We found that, in case of sulfide-undersaturated and volatile-rich arc basalts, metals are scarcely subtracted by degassing during ascent to shallow crustal reservoirs and reach the highest abundances in intermediate magmas (250 ppm Cu). At sulfide saturation the sulfide melt has 34–66 wt% Cu, leading to a dramatic decrease in chalcophile metals dissolved in the silicate melt. After fractionation of only 0.2–0.3 wt% of sulfide in the solid assemblage, the exsolved sulfide is a monosulfide solid solution (pyrrhotite) containing <3 wt% Cu. Metals that do not partition in sulfides (Pb, Zn) increase their concentrations during magmatic evolution until they are sequestered by a Cl-rich aqueous fluid phase exsolved at the rhyolitic stage. The absolute and Cu-normalized concentrations of metals in sulfide inclusions are similar to sulfide accessories in magmatic rocks associated with world-class porphyry Cu systems. Our results demonstrate that the mechanisms governing metal evolution inferred for the magmatic stage in porphyry Cu environments can be also tracked at an active arc volcano, using eruptive products as snapshots of the magmatic evolution. Arc volcanoes can thus be viewed as ideal active analogues when studying these crucial processes for the formation of porphyry Cu deposits.

1. Introduction

Metal evolution in arc magmas is difficult to constrain due to the loss of volatiles and the loss of metals during crystallization and because, in most cases, magmas become saturated in sulfides at some stage during their evolution (Audétat and Simon, 2012). Indeed, due to the strong affinity of chalcophile and siderophile elements (e.g., Platinum-Group Elements, Cu, Au, and Ag) for the sulfide phase, sulfides exsolved from silicate magmas lead to severe metal depletion in the residual silicate melt (Park et al., 2015).

A primary control on metal evolution in arc magmas is exerted by: 1) the timing of sulfide saturation relative to magmatic differentiation and volatile exsolution; 2) the amount of metal segregated into magmatic sulfides; 3) the amount of sulfide formed; 4) and whether sulfides are 'irretrievably lost' or may instead release metals again at later stages (Bai et al., 2020; Chang and Audétat, 2018; Halter et al., 2005; Hao et al., 2019; Mungall et al., 2015; Park et al., 2015, 2019; Wilkinson, 2013; Zhang and Audétat, 2017). The combined role of these factors has proven difficult to resolve, largely because of the complexity in measuring the metal content of the magmas during their evolution (Park et al., 2019). Information mostly derives from the roots - sulfide-bearing cumulates - of their plumbing system or from the mineralized bodies (Chang and Audétat, 2018; Chen et al., 2020). As magmatic-hydrothermal ore deposits can be considered the extinct equivalent of active magmatic systems (Hedenquist and Lowenstern, 1994), the investigation of these processes in the products of active arc volcanoes, particularly with the support of data from silicate melt inclusions, can provide pivotal information on metal budget and ore genetic models associated with arc-related magmas. A significant advantage in studying active volcanic systems is the lack of hydrothermal alteration or mineralization overprints, as shown by recent works for magmatic sulfide saturation studies (Fulignati et al., 2018; Georgatou et al., 2018; Georgatou and Chiaradia, 2020; Nadeau et al., 2010; Zelenski et al., 2018). Despite that, very few works have tackled the investigation of metal evolution through the processes of magma differentiation, sulfide exsolution

and fluid exsolution at active volcanoes or across the wide compositional spectra of magma types (Cox et al., 2019; Park et al., 2013, 2015; Timm et al., 2012).

La Fossa volcano (Italy) is an ideal site to study mineralizing processes beneath arc volcanoes, being characterized by an active magmatic-hydrothermal system (Boyce et al., 2007; Fulignati et al., 1998) and providing evidence of sulfide melt-silicate melt immiscibility (Fulignati et al., 2018). Here we use melt inclusions, magmatic sulfides and host minerals to track the evolution of metals for the entire basalt to rhyolite compositional spectrum. The suite belongs to a shoshonitic to potassic series in a subduction setting, similar to part of the magma types found in association with porphyry Cu deposits (Audétat and Simon, 2012; Sillitoe, 2010). Moreover, we compare our results to metal contents in sulfides from magmatic systems associated with ore deposits, showing that strong analogies exist between metal evolution in active arc volcanoes and those reported for porphyry Cu environments.

2. Geological background

La Fossa is the active volcanic center of Vulcano Island, in the Aeolian archipelago, a continental volcanic arc located in southern Tyrrhenian Sea (Fig. 1a, b). The volcanic activity of the island started at 130 ka with high-K calcalkaline (HKCA), shoshonitic (SHO) and, recently, potassic (KS) magmas (De Astis et al., 2000), showing the entire range in composition from basalt to rhyolite (Fig. 1c, d). The plumbing system of La Fossa is polybaric, dominated by fractional crystallization, crustal assimilation and magma mixing processes (Costa et al., 2020; De Astis et al., 2013; Peccerillo et al., 2006). These occur in a shoshonitic to latitic magma chamber at about 15 km deep, fed by shoshonitic basaltic magmas, and in shallower and smaller trachytic to rhyolitic reservoirs at 5–2 km deep (Costa et al., 2020; De Astis et al., 2013; Fulignati et al., 2018). Basaltic magmas have been only erupted at about 50 ka. They are H_2O-rich (water up to 5 wt%; Le Voyer et al., 2014) and oxidized. La Fossa has been quiescent since 1890 CE, with a high temperature fumarolic field fed by magmatic and hydrothermal fluids (Paonita et al., 2013). A similar hydrothermal system was active in the past, as testified by hydrothermally altered lithics found in the eruptive products of recent (post-1000 CE) eruptions (e.g. Breccia di Commenda eruption; Fulignati et al., 1998; Gurioli et al., 2012; Rosi et al., 2018).

3. Materials and analytical methods

Samples were selected to ensure that the entire range of magma types, from basalt to rhyolite, was included in this study. They were analyzed for the composition of their sulfide (SIs) and melt (MIs) inclusions hosted within phenocrysts. Samples were preferentially selected from explosive eruptions, targeted to ensure quenching of melt inclusions to a glass with the eruption. This minimizes the potential for post-entrapment crystallization of microlites in the trapped melt or crystallization of the host mineral on the inclusion walls. They include scoriaceous lapilli of La Sommata and Vulcanello, of basaltic and shoshonitic composition, respectively. The latitic, trachytic and rhyolitic samples are represented by the Palizzi eruptive period of La Fossa and consist of dark grey coarse ash of Pal A (latite) and Pal C (latite, trachyte), pumiceous lapilli of Pal D (trachyte) and Pal B (rhyolite), and the Palizzi lava flow (trachyte) (see De Astis et al., 2013 and Di Traglia et al., 2013 for further information on volcanic stratigraphy). Lapilli were crushed and crystals were hand-picked under a stereomicroscope, embedded in epoxy resin mounts and polished. Slices of the Palizzi lava flow sample were also prepared in epoxy resin mounts for petrographic investigations and microanalyses. The polished resin mounts were first studied under reflected light with a petrographic microscope at the Dipartimento di Scienze della Terra at the Università di Pisa. Melt and sulfide inclusions were identified for the analytical follow-up. To avoid post-entrapment modifications of the melt composition due to melt crystallization or leakage, the selected melt inclusions are entirely glassy (no microlites) and lack large vapor bubbles or other evidence of only partial enclosing by the host crystal. Shrinkage bubbles are absent or small in Vulcanello MIs while they are common in La Sommata basalt and in Palizzi trachyte; bubbles may host traces of volatile elements escaped from melt, but the observation that they are apparently empty means that we can consider their metal content negligible. Based on the inspection of MIs under back-scattered electron (BSE) microscopy and on their major element composition, post-entrapment crystallization of the host on the inclusion walls can also be considered negligible with respect to chalcophile metals. This is in agreement with previous estimates (<2 wt%) of olivine host crystallization for Vulcanello MIs (Fusillo et al., 2015), corresponding to a variation of the Cu content within analytical uncertainty.

After carbon-coating, backscattered electron images and the major element chemical composition of sulfide and melt inclusions were obtained with a Quanta 450 Field Emission-Scanning Electron Microscope (FE-SEM) (15 kV accelerating voltage, 10 mm working distance and 0.1 nA) equipped with Bruker microanalytical EDS system QUANTAX installed at the Centro Interdipartimentale di Scienza e Ingegneria dei Materiali (CISIM) at the Università di Pisa. Major and minor element compositions for each melt inclusion were also characterized using an electron probe microanalyzer (EPMA) JEOL JXA-8200, operating in wavelength dispersive mode with a defocused beam of 5 μm (15 kV accelerating voltage and 5 nA beam current) at the Dipartimento di Scienze della Terra at the Università di Milano.

The bulk major element compositions of the texturally non-homogeneous sulfide inclusions were reconstructed using spot analyses on the various sulfide phases present within each exposed sulfide inclusion. The reconstructed bulk composition was calculated dependent on the relative area percent of each sulfide phase, in the BSE images. Area percentages were determined using the image processing software package *ImageJ* (Image Processing and Analysis in Java, http://rsb.info.nih.gov/ij/) and the 2D images were segmented by manual thresholding. The uncertainty on the reconstructed bulk composition, involving both instrumental analytical error and manual image thresholding error, was evaluated to be <10%.

Trace element analyses of melt and sulfide inclusions and of host minerals were performed in situ by laser ablation inductively coupled plasma mass spectrometry (LA-ICPMS) at Géosciences Montpellier (Université de Montpellier, AETE-ISO regional facility of the OSU OREME), with a pulsed 193 nm ArF excimer laser (Analyte G2 from Teledyne) coupled to a Thermofinnigan Element XR mass spectrometer. For the analyses of host minerals, the laser was operated at a repetition rate of 8 Hz using spot sizes of 85 and 110 μm and a 6 J/cm^2 energy density. Total analysis time was 120 s with the first 80 s used for the background measurement and the last 40 s for sample ablation. Synthetic glass NIST 612 was used for external calibration. For melt inclusions, the laser was operated at a repetition rate of 6 Hz using spot sizes of 10 to 20 μm and a 6 J/cm^2 energy density. Total analysis time was 120 s with the first 80 s used for background measurement and the last 40 s for sample ablation. Synthetic glass NIST 610 was used for external calibration. For minerals and glass inclusions the accuracy of the analyses was monitored using the standard glass BIR-1 and SiO_2 of each mineral/glass, used as internal standard. For sulfide inclusions, only those where their exposed diameter was >15 μm were analyzed. The beam spot sizes were 5 to 10 μm. Only two non-homogeneous (polymineralic) sulfide inclusions were sufficiently large to be analyzed; the laser spot was tuned to approximate the "bulk" composition of the sulfide inclusion, without distinguishing among the single sulfide phases. The laser was operated at a repetition rate of 6 Hz using and a 6 J/cm^2 energy density with a total analysis time of 240 s (200 s for background measurement and 40 s of sample analysis). The Synthetic standard MASS-1 was used for external calibration. FeO (measured FeO, in the case of homogeneous sulfide inclusions, and FeO reconstructed with the above described procedure, in the case of non-homogeneous

polymineralic sulfide inclusions) was used as an internal standard. Data reduction for the mineral, melt and sulfide inclusion was performed with the software package Glitter (http://www.glitter-gemoc.com). Detection limits, results of reference materials and control standard analysis are provided in the Supplementary Material S1.

4. Results

4.1. Sulfide inclusions

Based on their textures (polymineralic and homogeneous), two types of sulfide inclusions (Type 1 SIs, polymineralic and Type 2 SIs, homogeneous) were identified in the Vulcano products. Both types are spherical when found in glass, and spherical or ovoid to elongated in shape when enclosed in host phenocrysts, with shape partially defined by surrounding crystal growth (Fig. 2a).

Type 1 SIs (17 inclusions) are between 1 and 20 μm in diameter (mostly <10 μm) and consist of two or three Cu-rich sulfide phases each (Fig. 2a). These SIs are hosted in clinopyroxene, magnetite and feldspars (Fig. 2b). The composition of Type 1 sulfides (Table 1), when plotted in a Cu-Fe-S diagram at 1000 °C (Fig. 2c), spans from *bornite solid solution* (*bnss*) to the sulfide liquid field (*SL*). The reconstructed bulk composition of these unmixed SIs ranges from 66 wt% to 34 wt% Cu in the Cu-Fe-S diagram (Fig. 2c). Trace elements were measured up to 493 ppm Ni, 131 ppm Co, 1145 ppm Zn, 397 ppm As, 208 ppm Se, 354 ppm Ag and 2020 ppm Pb (Table 2) within the two Type 1 SIs analyzed (which contained 65 and 46 wt% Cu).

Type 2 SIs (59 inclusions) are 5–60 μm in diameter with a mean size of 20 μm and homogeneous textures (Fig. 2a); they occur in clinopyroxene, olivine, Ti-magnetite, plagioclase, sanidine, biotite and glass and prevail in mafic phases and glass. Type 2 SIs plot, at 1000 °C, in the pyrrhotite field (*mss*, monosulfide solid solution), with Cu content up to 2.6 wt% (Fig. 2c; Table 1). If compared to Type 1 SIs, they show markedly higher Ni and Co contents, up to 3495 ppm and 4248 ppm, respectively, similar Zn and lower Pb (up to 385 ppm), with Ag and Se, in

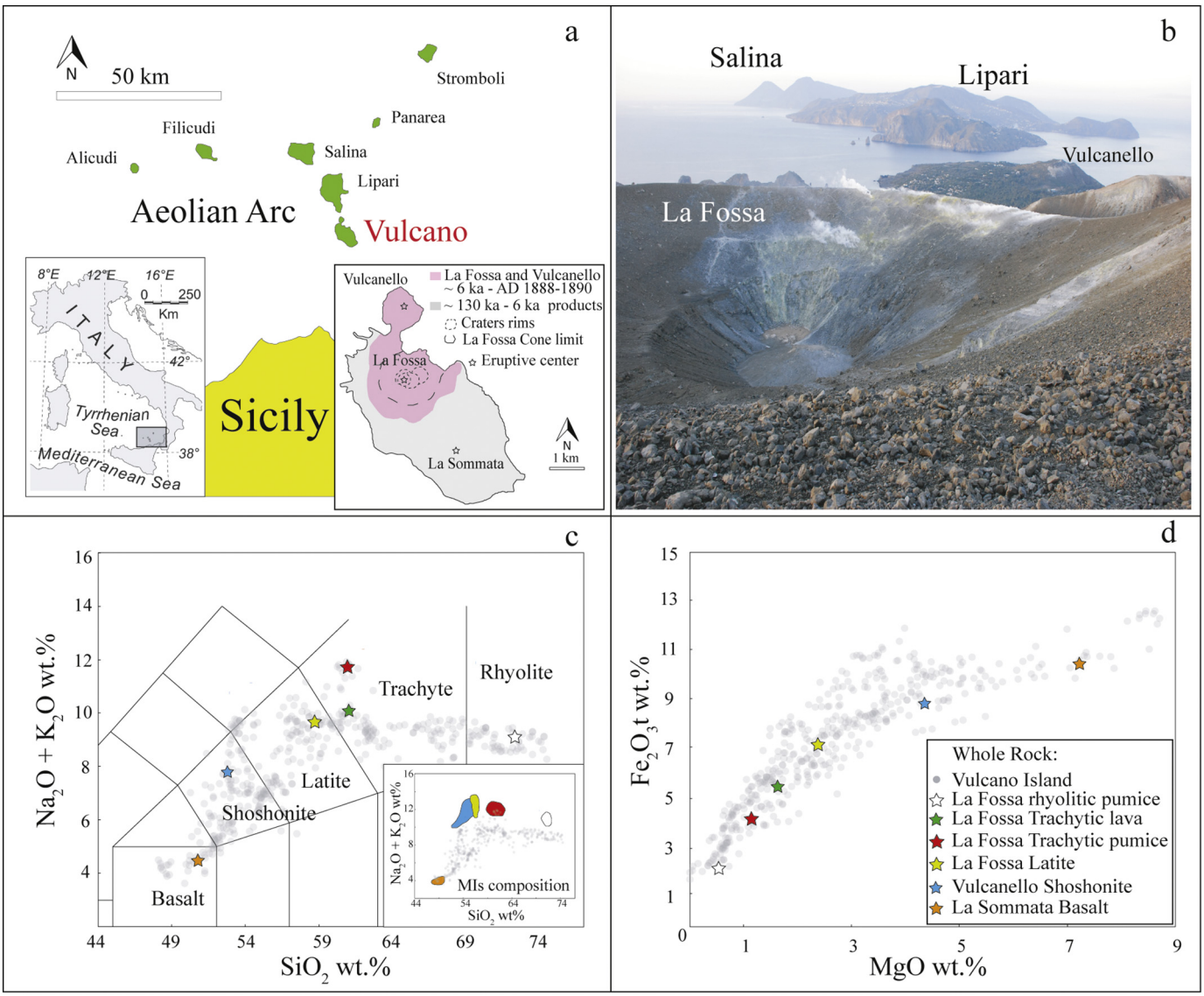

Fig. 1. (a) Location of La Fossa volcano and Vulcano island in the Aeolian Arc; (b) Panoramic view toward N of La Fossa crater and its fumarolic field; (c) TAS (total alkali vs SiO_2) diagram of Vulcano rocks. Stars are the samples selected to represent the basalt to rhyolite suite; insert in (c) shows the composition of MIs of the selected samples; (d) Fe_2O_3 tot. vs MgO diagram of Vulcano products. Whole rock data in (c) and (d) are re-calculated to 100 on anhydrous basis; literature data are from De Astis et al. (2013), Fusillo et al. (2015) and Costa et al. (2020). Melt inclusions major elements data are from Gioncada et al. (1998), Le Voyer et al. (2014), Fusillo et al. (2015), Fulignati et al. (2018) and this work. The complete data set of MIs is reported in the supplementary material S1.

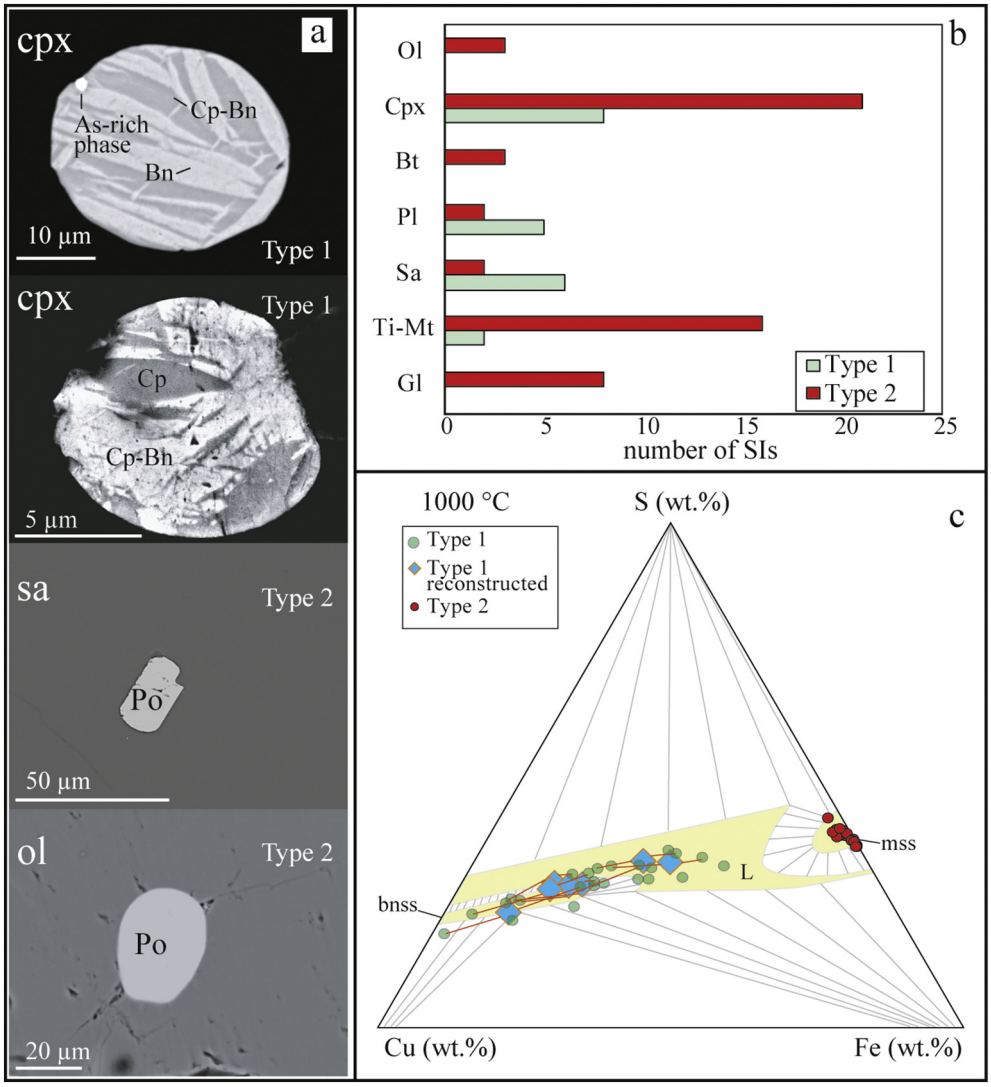

Fig. 2. (a) BSE images of Type 1 SIs consisting of unmixed chalcopyrite (Cp)-bornite (Bn) and Type 2 SIs represented by homogeneous pyrrhotite (Po); (b) abundance of SIs in the various mineral phases and groundmass glass of eruptive products (Ol: olivine; Cpx: clinopyroxene; Bt: biotite; Pl: plagioclase; Sa: sanidine; Mt.: magnetite; Gl: groundmass glass); (c) Composition of SIs in the Cu-Fe-S system at 1000 °C (Craig and Kullerud, 1969), for Type 1 SIs analyses of unmixed phases and the correspondent reconstructed composition are shown and joined by red lines, error bars fall within the symbols; data from this work and Fulignati et al. (2018) are reported in Table 1 and in the supplementary material S1. L, liquid; bnss, bornite solid solution; mss, monosulfide solid solution. (For interpretation of the references to colour in this figure legend, the reader is referred to the web version of this article.)

the tens of ppm range. The only SI found in a rhyolite is pyrrhotite with 0.4 wt% Cu, characterized by very low Zn, Pb and Ag and higher Mo contents (Tables 1 and 2).

Type 1 and Type 2 SIs are common accessories in trachytes, whereas they are extremely rare in latites (only Type 1 SIs) and in rhyolites (only Type 2 SIs), where just a couple of SIs were found after the inspection of several dozens of crystals. They are absent in basalt-shoshonite rocks. The two types of SIs never coexist in the samples of the same eruption. The entire dataset of analyses of the sulfides and hosts are reported in Tables 1 and 2 and Supplementary Material S1.

Some differences can be found when comparing the host mineral compositions for Type 1 and Type 2 SIs. Clinopyroxene (the most frequent host for both types of SIs; Fig. 2b) shows higher Cu, Cr, V and Ni contents for Type 1 sulfides compared to Type 2, for a similar Mg# range (see Supplementary Material S1). This is confirmed also when comparing the entire clinopyroxene analytical dataset (Supplementary Material S1) for the Vulcano products hosting Type 1 and Type 2 SIs.

4.2. Melt inclusions

The composition of glassy MIs in olivine, clinopyroxene, plagioclase, sanidine and biotite found in the products of explosive eruptions of basaltic, shoshonitic, latitic, trachytic and rhyolitic magmas is assumed to be representative of the magmas spanning the whole La Fossa magmatic differentiation path (Fig. 1c, Table 3 and Supplementary Material S1). The differentiation trend involves the fractionation of olivine, clinopyroxene, Ti-magnetite, labradorite to andesine plagioclase and, in evolved magmas, sanidine, minor oligoclase and biotite (Gioncada et al., 1998). Ti-magnetite joins the fractionating assemblage early, as shown by the decrease of Fe with Mg (Fig. 1d), while apatite joins later in intermediate terms.

The Cu content of MIs reaches the highest values at intermediate compositions (Zr around 160–200 ppm, at the latite-trachyte transition) and, when the highest Cu contents are considered, defines a trend that increases with magmatic differentiation from basalt (~50 ppm) to latite and trachyte (~250 ppm), and then abruptly drops to <60 ppm (Fig. 3a). Low Cu values have also been measured in

t1.1 **Table 1**

t1.2 Major element composition (wt%) of Type 1 and Type 2 SIs; Ol: olivine; Cpx: clinopyroxene; Bt: biotite; Pl: plagioclase; Sa: sanidine; Ti-Mt: Ti-magnetite. Reconstructed: calculated bulk

t1.3 composition of the sulfide inclusions (see methods section for details and supplementary materials for phase proportions); bdl: below detection limit; source a: Fulignati et al. (2018),

t1.4 EPMA analyses; source b: this work, FE-SEM-EDS analyses.

t1.5	Host rock	Unit	Host mineral	Sulfide ID	Sulfide type	Source	Fe	S	Co	Mn	Ni	Zn	Cu	Total
t1.6	Trachyte	Pal D	sa	PAL-90 sulf1	2	a	58.48	37.19	0.09	0.08	0.06	bdl	1.44	97.33
t1.7	Trachyte	Pal D	cpx	PAL-90 sulf2	2	a	59.12	38.05	0.03	0.09	0.03	0.10	1.19	98.60
t1.8	Trachyte	Pal D	cpx	PAL-90 sulf2	2	a	59.89	38.08	0.07	0.12	0.05	0.03	0.42	98.65
t1.9	Trachyte	Pal D	ol	pal90solf3	2	a	57.19	37.24	0.14	0.18	0.07	0.07	1.62	96.52
t1.10	Trachyte	Pal D	gl	pal90solf4	2	a	58.01	37.24	0.16	0.11	0.09	bdl	2.32	97.93
t1.11	Trachyte	Pal D	ol	pal90solf5	2	a	58.94	37.60	0.10	0.12	0.10	bdl	1.67	98.53
t1.12	Trachyte	Pal D	ol	pal90solf5	2	a	59.19	38.08	0.09	0.18	0.04	bdl	1.29	98.88
t1.13	Trachyte	Pal D	gl	pal90sulf8	2	a	57.09	38.05	0.07	0.10	0.04	0.11	1.34	96.80
t1.14	Trachyte	Pal D	Ti-mt	pal90sulf10	2	a	58.72	38.24	0.05	0.16	0.05	0.05	0.97	98.23
t1.15	Trachyte	Pal D	cpx	pal90sulf13	2	a	58.38	37.99	0.13	0.12	0.00	0.03	1.54	98.18
t1.16	Trachyte	Pal D	cpx	pal90sulf13	2	a	58.25	37.70	0.07	0.04	0.01	0.06	1.46	97.58
t1.17	Trachyte	Pal D	cpx	pal90sulf14a	2	a	53.30	39.64	0.14	0.09	0.06	bdl	2.16	95.39
t1.18	Trachyte	Pal D	Ti-mt	PAL90 u293sulf17	2	a	58.15	37.73	0.09	0.08	0.01	bdl	1.31	97.37
t1.19	Trachyte	Pal D	Ti-mt	PAL90 u293sulf17	2	a	58.60	38.26	0.07	0.12	0.09	0.02	1.39	98.54
t1.20	Trachyte	Pal D	pl	PAL90U297 sulf18	2	a	56.63	37.48	0.03	0.10	0.08	0.10	1.55	95.95
t1.21	Trachyte	Pal D	cpx	PAL-15D sulf1	2	a	56.33	37.35	0.11	0.11	0.04	bdl	1.34	95.28
t1.22	Trachyte	Pal D	cpx	PAL-15D sulf2	2	a	57.60	37.53	0.12	0.13	0.05	bdl	1.32	96.75
t1.23	Trachyte	Pal D	Ti-mt	PAL-15D sulf3	2	a	56.48	37.45	0.13	0.12	0.05	0.04	1.34	95.60
t1.24	Trachyte	Pal D	gl	PAL-15D sulf4	2	a	56.85	37.61	0.09	0.11	0.05	0.11	1.30	96.12
t1.25	Trachyte	Pal D	cpx	sulf5	2	a	56.06	37.68	0.06	0.14	0.06	bdl	1.84	95.84
t1.26	Trachyte	Pal D	cpx	pal15sulf8.spc	2	a	57.15	37.63	0.04	0.13	bdl	0.04	1.02	96.00
t1.27	Trachyte	Pal D	cpx	Pal 15 D sulf 6	2	a	56.28	37.64	0.08	0.10	0.05	0.06	2.51	96.71
t1.28	Trachyte	Pal D	cpx	Pal 15 D sulf 6	2	a	56.35	37.64	0.14	0.12	0.11	0.11	2.54	97.01
t1.29	Trachyte	Pal D	cpx	Pal 15 D sulf 6	2	a	56.40	37.67	0.15	0.01	0.07	0.07	2.72	97.09
t1.30	Trachyte	Pal D	Ti-mt	Pal 15 D sulf 7	2	a	57.99	37.64	0.03	0.10	0.05	0.04	1.21	97.06
t1.31	Trachyte	Pal D	Ti-mt	Pal 15 D sulf 8	2	a	57.96	37.57	0.12	0.11	0.08	0.04	1.58	97.46
t1.32	Trachyte	Palizzi lava	pl	SC15-1_1	1	b	24.05	32.12	bdl	bdl	bdl	bdl	43.83	100.00
t1.33	Trachyte	Palizzi lava	pl	SC15-1_1	1	b	38.65	33.84	bdl	bdl	bdl	bdl	27.51	100.00
t1.34	Trachyte	Palizzi lava	pl	reconstructed *SC15-1_1	1	b	33.54	33.24	bdl	bdl	bdl	bdl	33.22	100.00
t1.35	Trachyte	Palizzi lava	pl	SC15-1_2	1	b	21.84	31.58	bdl	bdl	bdl	bdl	46.58	100.00
t1.36	Trachyte	Palizzi lava	pl	SC15-1_2	1	b	33.72	34.57	bdl	bdl	bdl	bdl	31.70	100.00
t1.37	Trachyte	Palizzi lava	pl	reconstructed *SC15-1_2	1	b	28.50	33.25	bdl	bdl	bdl	bdl	38.25	100.00
t1.38	Trachyte	Palizzi lava	cpx	SC15-1_3	1	b	20.92	28.88	bdl	bdl	bdl	bdl	50.20	100.00
t1.39	Trachyte	Palizzi lava	cpx	SC15-1_3	1	b	5.09	22.51	bdl	bdl	bdl	bdl	72.40	100.00
t1.40	Trachyte	Palizzi lava	cpx	SC15-1_3	1	b	20.74	30.62	bdl	bdl	bdl	bdl	48.64	100.00
t1.41	Trachyte	Palizzi lava	cpx	reconstructed *SC15-1_3	1	b	15.57	27.94	bdl	bdl	bdl	bdl	56.48	100.00
t1.42	Trachyte	Palizzi lava	cpx	SC15-1_3b	1	b	21.60	23.91	bdl	bdl	bdl	bdl	54.49	100.00
t1.43	Trachyte	Palizzi lava	cpx	SC15-1_3b	1	b	12.40	21.58	bdl	bdl	bdl	bdl	66.02	100.00
t1.44	Trachyte	Palizzi lava	cpx	SC15-1_4	1	b	37.20	29.81	bdl	bdl	bdl	bdl	32.99	100.00
t1.45	Trachyte	Palizzi lava	cpx	SC15-1_4	1	b	30.91	31.85	bdl	bdl	bdl	bdl	37.24	100.00
t1.46	Trachyte	Palizzi lava	pl	SC15-1_5	1	b	10.02	25.69	bdl	bdl	bdl	bdl	64.29	100.00
t1.47	Trachyte	Palizzi lava	pl	SC15-1_5	1	b	22.46	29.18	bdl	bdl	bdl	bdl	48.36	100.00
t1.48	Trachyte	Palizzi lava	pl	reconstructed *SC15-1_5	1	b	20.64	28.67	bdl	bdl	bdl	bdl	50.69	100.00
t1.49	Trachyte	Palizzi lava	pl	SC15-1_6	1	b	18.07	30.59	bdl	bdl	bdl	bdl	51.35	100.00
t1.50	Trachyte	Palizzi lava	pl	SC15-1_6	1	b	9.64	24.69	bdl	bdl	bdl	bdl	65.66	100.00
t1.51	Trachyte	Palizzi lava	pl	reconstructed *SC15-1_6	1	b	15.62	28.88	bdl	bdl	bdl	bdl	55.50	100.00
t1.52	Trachyte	Pal D	sa	SC_18_20c1	2	b	62.38	37.48	bdl	bdl	bdl	bdl	0.14	100.00
t1.53	Trachyte	Pal D	sa	SC_18_20c2	2	b	62.83	36.85	bdl	bdl	bdl	bdl	0.32	100.00
t1.54	Trachyte	Pal D	sa	SC_18_20c3	2	b	62.18	37.21	bdl	bdl	bdl	bdl	0.60	100.00
t1.55	Trachyte	Pal D	sa	SC_18_20c4	2	b	63.61	36.11	bdl	bdl	bdl	bdl	0.28	100.00
t1.56	Trachyte	Pal D	pl	SC_18_20c5	2	b	63.70	36.20	bdl	bdl	bdl	bdl	0.10	100.00
t1.57	Trachyte	Palizzi lava	Ti-mt	sc1824 11–12	1	b	24.18	28.79	bdl	bdl	bdl	bdl	47.04	100.00
t1.58	Trachyte	Palizzi lava	Ti-mt	sc1824 11–12	1	b	31.37	29.73	bdl	bdl	bdl	bdl	38.91	100.00
t1.59	Trachyte	Palizzi lava	cpx	sc1824 4–5-6	1	b	20.42	28.20	bdl	bdl	bdl	bdl	51.38	100.00
t1.60	Trachyte	Palizzi lava	cpx	sc1824 4–5-6	1	b	2.27	18.68	bdl	bdl	bdl	bdl	79.05	100.00
t1.61	Trachyte	Palizzi lava	cpx	reconstructed *sc1824 4–5-6	1	b	10.89	23.21	bdl	bdl	bdl	bdl	65.90	100.00
t1.62	Trachyte	Palizzi lava	cpx	sc1824 7–8	1	b	29.89	29.63	bdl	bdl	bdl	bdl	40.48	100.00
t1.63	Trachyte	Palizzi lava	cpx	sc1824 7–8	1	b	22.97	28.30	bdl	bdl	bdl	bdl	48.73	100.00
t1.64	Trachyte	Palizzi lava	cpx	reconstructed *sc1824 7–8	1	b	25.18	28.73	bdl	bdl	bdl	bdl	46.09	100.00
t1.65	Latite	Pal C	Ti-mt	sulf n4	1	b	28.65	32.34	bdl	bdl	bdl	bdl	39.01	100.00
t1.66	Latite	Pal C	Ti-mt	solf n4	1	b	11.75	25.37	bdl	bdl	bdl	bdl	62.88	100.00
t1.67	Latite	Pal C	Ti-mt	reconstructed *solfn4	1	b	18.51	28.15	bdl	bdl	bdl	bdl	53.34	100.00
t1.68	Rhyolite	Pal B	sa	pallentiasulf1	2	a	59.58	36.72	0.03	0.03	0.04	0.09	0.33	96.81
t1.69	Rhyolite	Pal B	sa	pallentiasulf1	2	a	58.57	36.56	0.04	0.07	0.01	bdl	0.42	95.67

some intermediate composition MIs. Conversely, Pb concentration in MIs increases from basalt (5 ppm) to trachyte (35 ppm) and remains constant in rhyolites (Fig. 3b).

The average metal concentrations measured in Type 2 SIs (Table 2) and in coexistent MIs (Table 4) allow the sulfide phase/silicate melt partition coefficients for Cu (1184), Ni (352), Zn (1.25), V (3.17), Pb (1.77) to be calculated. The sulfide phase/silicate melt partition coefficients for the same metals in Type 1 sulfides, mostly lacking coexistent melt inclusions, are determined assuming the average Cu content of latitic-trachytic melt inclusions (Table 4) and are 1538 for Cu, 154 for Ni, 1.32 for Zn, 1.8 for V and 76 for Pb.

Table 2

Major and trace elements (ppm) bulk composition of Type 1 and Type 2 SIs analyzed by LA-ICP-MS; Ol: olivine; Cpx: clinopyroxene; Sa: sanidine; Ti-Mt: Ti-magnetite.

Host rock	Unit	Host mineral	Sulfide ID	Sulfide type	S	V	Mn	Fe	Co	Ni	Cu	Zn	As	Se	Mo	Ag	Cd	Sn	Sb	Te	Pt	Au	Tl	Pb	Bi
Trachyte	Pal D	sa	PAL-90 sulf1	2	371,919	bdl	671	676,629	823	269	17,048	241	bdl	25.84	0.47	3.98	1.16	2.05	0.18	bdl	0.08	0.01	0.07	3.90	bdl
Trachyte	Pal D	cpx	PAL-90 sulf2	2	380,658	8.80	275	249,572	362	111	6626	378	bdl	2.21	bdl	3.46	bdl	3.47	bdl	bdl	0.48	bdl	0.01	4.38	0.08
Trachyte	Pal D	ol	pal90solf5	2	378,390	1.39	493	454,061	1406	690	35,369	150	bdl	183.55	1.67	3.43	3.85	bdl	0.06	bdl	0.02	0.14	60.27	4.50	0.13
Trachyte	Pal D	Ti-mt	pal90sulf10	2	382,459	170	762	690,365	593	85	17,666	314	34.08	bdl	26.79	2.21	1.16	bdl	0.12	1.67	0.51	bdl	4.06	194	78.4
Trachyte	Pal D	cpx	pal90sulf13	2	378,456	24.98	1202	533,044	1701	380	20,826	157	3.19	bdl	2.78	4.13	0.46	1.41	1.00	1.23	bdl	0.26	1.35	3.27	0.14
Trachyte	Pal D	cpx	pal90sulf14a	2	396,402	6.23	795	695,233	1334	354	29,342	230	bdl	bdl	3.81	3.22	0.50	1.07	bdl	bdl	0.08	0.10	0.07	3.08	0.17
Trachyte	Pal D	Ti-mt	PAL90 u293sulf17	2	379,924	85.56	797	445,303	1107	153	11,738	294	3.32	78.58	2.31	2.28	0.16	2.77	bdl	bdl	bdl	0.04	1.09	35.01	0.71
Trachyte	Pal D	Ti-mt	PAL90 u293sulf17	2	379,924	32.83	746	459,804	869	185	10,467	243	8.76	bdl	7.57	2.19	3.60	0.94	bdl	0.37	bdl	bdl	0.49	19.60	10.8
Trachyte	Pal D	cpx	PAL-15D sulf1	2	149,585	1068	39,728	582,983	1438	1145	6334	1664	bdl	84.77	0.20	17.52	bdl	16.35	bdl	2.31	bdl	bdl	bdl	12.81	0.85
Trachyte	Pal D	cpx	PAL-15D sulf2	2	341,034	119	6800	582,983	2627	2917	13,900	603	2.11	4.71	2.09	3.68	4.18	0.48	bdl	2.00	0.13	0.18	0.03	4.15	0.30
Trachyte	Pal D	cpx	sulf5	2	346,344	206	12,951	582,983	2412	375	10,979	1445	bdl	107	2.36	9.86	10.95	4.96	0.99	bdl	0.29	0.04	0.20	6.64	0.38
Trachyte	Pal D	cpx	Pal 15 D sulf 6	2	370,083	1.66	3026	582,983	4248	3495	24,755	433	bdl	48.50	1.68	1.87	1.31	0.93	bdl	0.48	0.18	0.18	0.35	14.51	7.60
Trachyte	Pal D	cpx	Pal 15 D sulf 6	2	232,691	132	2413	582,983	1550	2145	12,373	644	50.61	15.36	22.58	13.36	6.27	bdl	1.82	1.52	0.34	0.46	7.18	384.56	166
Trachyte	Pal D	Ti-mt	Pal 15 D sulf 7	2	422,053	712	3501	582,983	3248	2661	15,932	1006	bdl	bdl	2.12	6.36	1.07	1.29	bdl	bdl	0.10	0.11	0.45	4.66	0.23
Trachyte	Pal D	Ti-mt	Pal 15 D sulf 8	2	349,260	314	2605	582,983	3377	3397	16,455	830	bdl	11.01	1.72	3.74	1.60	3.16	bdl	bdl	0.12	0.07	0.32	3.72	0.12
Trachyte	Palizzi lava	cpx	sc1824 4–5-6	1	595,243	117	1505	173,263	59	47	1,193,582	1145	397.31	208	6.46	354.05	0.64	14.27	4.93	0.50	0.07	bdl	0.03	34.41	3.31
Trachyte	Palizzi lava	cpx	sc1824 7–8	1	148,141	0.05	682	108,824	131	493	248,441	607	0.47	15.66	0.02	9.07	16.64	3.95	0.11	1.14	bdl	0.04	0.03	2020	32.6
Rhyolite	Pal B	sa	pallentiasulf1	2	362,456	bdl	1616	582,983	1216	1979	8003	44	bdl	45.77	76.36	1.85	2.14	1.83	bdl	3.41	bdl	0.03	0.12	0.80	0.23

5. Discussion

5.1. Evolution of metals in the magmas

The petrographic features and the chemical compositions of MIs and SIs found in Vulcano eruptive products allow the evolution of metals in the magmatic system of an active arc volcano to be tracked from basalt to rhyolite. This system is fed by sulfide-undersaturated, H_2O-rich and oxidized basaltic magmas. The first appearance of SIs indicates that sulfide saturation occurs late, during magma evolution, at the latite-trachyte transition. Accordingly, the fO_2 value decreases from basalts (NNO-NNO + 1) to intermediate magmas (trachyte magma ΔNNO -1 to −2; Fulignati et al., 2018). This is potentially due to the combined effects of lower temperatures, the fractionation of Fe-bearing minerals and the volatile loss during differentiation (Richards, 2015; Scaillet and MacDonald, 2006; Scaillet and Pichavant, 2005). At Vulcano island, sulfide saturation is unrelated to the sudden onset of magnetite crystallization ("magnetite crisis", Jenner et al., 2010), because magnetite fractionation starts early, while sulfide saturation is late.

Magmatic sulfide inclusions could be trapped either as a liquid (SL) or as a solid, which can be either a monosulfide solid solution (*mss*) or an intermediate solid solution (*iss*), having a composition close to pyrrhotite and chalcopyrite, respectively (Parat et al., 2011). For most metals, the partition coefficient between sulfide and silicate melt strongly depends on the nature of the sulfide phase (*mss*, *iss*, or SL; Li and Audétat, 2015). Thus, determining the nature of the sulfide phases at the time of trapping is important to constrain the metal budget of the magmatic system (Rottier et al., 2019 and references therein). By plotting both Type 1 and Type 2 SIs analyses on the ternary diagram of the Cu-Fe-S system (at 1000 °C), the reconstructed Type 1 SIs compositions fall in the liquid field, whereas Type 2 SIs fall in the pyrrothite (*mss*) field, suggesting that the latter were trapped as a solid phase. This evidence is supported by comparing their sulfide phase-silicate melt partition coefficients (for Cu, Ni, Pb, Zn), calculated from measured concentrationsandpredictedaccordingtotheequationsfor$D^X_{SL/SM}$, $D^X_{mss/SM}$ of Li and Audétat (2015) for a trachyte melt with 950 °C, ΔFMQ −0.77 and FeO 4.4 wt%. The comparison shown in Fig. 4 demonstrates a good match for both the Type 1 and the Type 2 SIs (these elements were selected because they could be reliably quantified in both magmatic sulfide and silicate melt inclusions, and because their partition coefficient is markedly different for *mss* versus SL). The different partition coefficients SL/SM and *mss*/SM are also in agreement with the measured Ag and Pb contents, which are considerably higher in Type 1 SIs than in Type 2 SIs.

The Cu behavior in the silicate melt confirms late sulfide saturation (Fig. 3a). In fact, Cu concentration in MIs increases from basalt to latite melts, which are sulfide-undersaturated, and then rapidly decreases within a narrow compositional interval (Zr 180–200 ppm; SiO_2 58–60 wt%) once sulfide saturation is reached, due to the stripping of Cu by Cu-rich sulfide melt. The scattered Cu concentrations, including very low values in the intermediate composition MIs range, might suggest that: (i) incipient sulfide saturation was achieved in some parts of the reservoir (at the contact with wall rock thanks to temperature decrease, fractional crystallization or silica assimilation?) although not revealed by sulfide trapping; (ii) Cu was episodically lost to a S-rich vapor phase from mafic magmas. Events of refilling by Cu-poor, S-rich and sulfide undersaturated magma could furthermore enhance the heterogeneity in the Cu content of an intermediate composition reservoir. This is particularly crucial because, in order to represent the entire basalt to rhyolite differentiation range, we analyzed samples that do not necessarily represent the evolution in a single reservoir but rather come from multiple, possibly independent magma batches with variable age.

The evolution of Cu and Pb in the silicate melt has been modeled with fractional crystallization, starting from a mean value of the La Sommata basaltic MIs and including a sulfide phase in the fractionating assemblage at the latite-trachyte stage (Fig. 3a, b). For this study, we

t3.1 **Table 3**

t3.2 Mean composition and standard deviation (SD) for major elements (wt%) of MIs in the Vulcano products. Literature EPMA data: Gioncada et al. (1998), Le Voyer et al. (2014) for La

t3.3 Sommata basalt; Fusillo et al. (2015) for Vulcanello 1 shoshonite; Fulignati et al. (2018) for Pal D trachyte. Pal C latite and Pal B rhyolite are FE-SEM-EDS analyses from this work.

t3.4 Host rock composition	Unit		SiO_2	TiO_2	Al_2O_3	FeO_t	MnO	MgO	CaO	Na_2O	K_2O	P_2O_5	Cl
t3.5 Basalt	La Sommata	mean (15)	45.91	0.62	10.99	8.93	0.17	8.76	14.34	1.99	1.85	0.31	0.29
t3.6		SD	0.80	0.06	0.40	0.49	0.02	1.36	0.49	0.17	0.28	0.20	0.05
t3.7 Shoshonite	Vulcanello 1	mean (33)	54.34	0.63	17.31	7.05	0.15	2.16	4.51	4.57	6.83	0.66	0.30
t3.8		SD	1.44	0.09	0.63	0.90	0.04	0.59	0.89	0.34	0.66	0.12	0.03
t3.9 Latite	Pal C	mean (5)	56.55	0.86	18.08	6.18	0.14	1.10	3.39	4.94	7.93	0.40	0.42
t3.10		SD	1.09	0.15	0.80	1.59	0.13	0.24	0.77	0.39	1.01	0.15	0.09
t3.11 Trachyte	Pal D	mean (22)	60.00	0.58	17.38	4.41	0.14	1.01	2.49	4.59	6.82	0.20	0.38
t3.12		SD	0.86	0.12	0.56	0.57	0.06	0.32	0.54	0.54	1.04	0.08	0.06
t3.13 Rhyolite	Pal B	mean (18)	70.44	0.13	14.87	2.02	0.11	0.13	0.95	4.53	6.64	0.06	0.51
t3.14		SD	0.79	0.05	0.62	0.29	0.05	0.11	0.16	0.48	0.51	0.00	0.08

neglected crustal assimilation processes. The model employs bulk distribution coefficient for Zr, Cu and Pb, calculated for each step of the differentiation process using partition coefficients derived from the literature and the relative proportions of crystallizing phases for Vulcano (Costa et al., 2020; see Supplementary Material S1 for details of the model). The sulfide phase/silicate melt partition coefficients for Pb and Cu were calculated according to Li and Audétat (2015) (Supplementary Material S1).

The models provide a robust explanation of the Cu behavior in the silicate melt. The fractional crystallization models predict that 0.2–0.3 wt% of sulfide melt fractionated along with clinopyroxene + plagioclase + Ti-magnetite + olivine + biotite + sanidine. This is sufficient to cause a sharp drop in the Cu content of silicate melt at the latite to trachyte transition. Because Type 1 and Type 2 SIs were never found to coexist, we suggest that the first sulfides formed at the highest Cu content are correspondingly Cu-rich (Type 1 SIs), whereas those exsolved from the Cu-depleted trachytic magma are the Cu-poor Type 2 SIs (Cu-bearing *mss*) found in trachyte and rhyolite (Fig. 3a). This reconstruction is in agreement with the composition of clinopyroxene crystals in the latites and trachytes. Clinopyroxene composition testifies that, in the latite-to-trachyte transition, the Cu-depleted trachytic magma is slightly more evolved (that is, having a lower Cr, V and Ni content in clinopyroxenes) than the Cu-rich trachyte and latite (Fig. 5). The trachyte-rhyolite step requires a high percentage (60 vol%) of fractionated solid (Costa et al., 2020), strongly increasing the final concentration of incompatible elements and possibly explaining the large spread in Zr values measured in rhyolites.

The evolution of Pb shows an increase with differentiation up to rhyolite (Fig. 3b). This agrees well with the low sulfide melt/silicate melt partition coefficient for this element, which is orders of magnitude lower than that of Cu (this work and Li and Audétat, 2015). The modeled Pb trend in rhyolites (Zr > 200 ppm), despite the higher D_{Pb}, slightly deviates from the measured data. This may be ascribed to the partitioning of Pb in an exsolved Cl-bearing aqueous fluid.

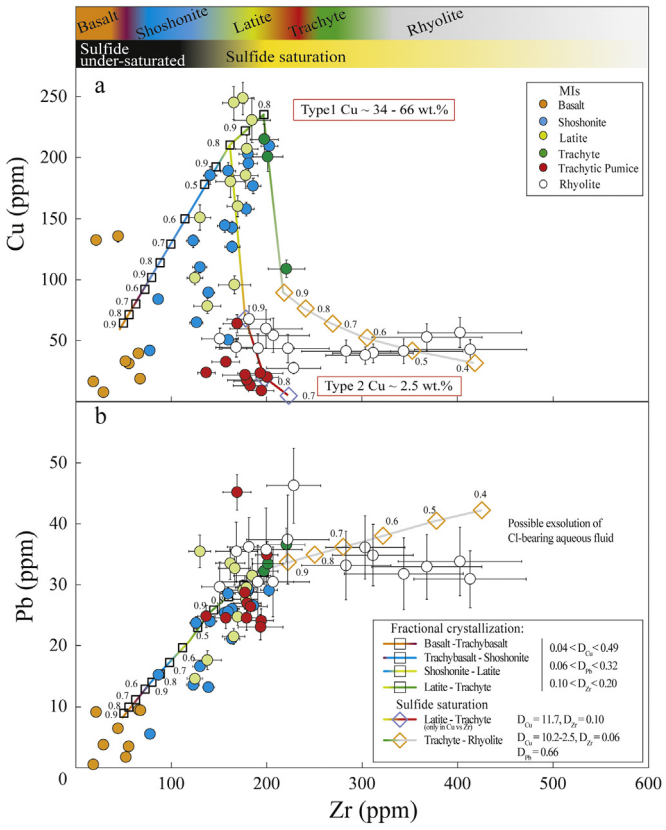

Fig. 3. Copper (a) and Pb (b) versus Zr as differentiation index for the glassy MIs representative of the basalt to rhyolite suite at Vulcano, with quantitative fractional crystallization model for the evolution of Cu and Pb in the silicate melt. Bulk partition coefficients (D) for Cu, Pb and Zr have been calculated using minerals/silicate melt partition coefficients from literature and sulfide/silicate melt partition coefficients calculated with the model of Li and Audétat (2015). See supplementary material S1 for additional details. 1 sigma error for each analysis is shown as error bars, which if not visible, is smaller than the symbol. Symbols and numbers along the fractionation paths indicate melt fraction.

5.2. The effect of fluid saturation

Tracking metal evolution in magmas cannot overlook the effect of fluid-saturation along differentiation. While Vulcano basalts are H_2O-, S-, Cl-rich, the shoshonitic magmas have lower volatile contents (Gioncada et al., 1998), suggesting that H_2O, S and Cl may be lost to an exsolved aqueous fluid phase at the basalt-shoshonite transition. Our results show that, despite mafic magmas degassing during ascent, Cu and Pb increase with differentiation (Fig. 3a, b). This suggests that the evolution of these metals is not significantly affected by decompression degassing of mafic magmas as they refill crustal reservoirs. Indeed, Cu scarcely partitions into a hydrosaline fluid phase exsolved from mafic magmas according to the experimental results of Zajacz et al. (2012).

In trachytes and rhyolites, the Cu-normalized abundances of S, Mo, Zn, Ag, Pt, Au, Pb in Type 1 (trachyte) and Type 2 (trachyte and rhyolite) SIs show different patterns (Fig. 6). While Mo/Cu ratio in the rhyolite Type 2 SIs is higher than that of Type 2 SIs in trachyte, Zn/Cu and Pb/Cu are distinctly lower (Fig. 6a). This is in agreement with the exsolution of a Cl-rich magmatic fluid phase from the rhyolitic magma at La Fossa (Fulignati et al., 2018), causing Pb and Zn to preferentially partition with respect to Mo (Zajacz et al., 2008). Mo, which is not efficiently partitioned in a Cl-rich magmatic fluid phase (Candela and Holland, 1984; Zajacz et al., 2008), tends to also increase in the rhyolite SIs.

At Vulcano, previous data suggest that metal-bearing fluids can be involved in phreatic-phreatomagmatic eruptions (Gurioli et al., 2012). An example is the Breccia di Commenda eruption, a violent explosive

Table 4

Trace elements composition (ppm) of MIs analyzed by LA-ICP-MS; B: La Sommata basalts; SH: Vulcanello 1 shoshonite; LT: Pal A and Pal C latites; TR: Pal C and Pal D trachytes; RH: Pal B rhyolite. Ol: olivine; Cpx: clinopyroxene; Sa: sanidine; bdl: below detection limit. Detection limits are in Supplementary Material S1.

MI id	Host mineral	V	Cr	Ni	Cu	Zn	Rb	Sr	Y	Zr	Nb	Cs	Ba	La	Ce	Pr	Nd	Sm	Eu	Gd	Tb	Dy	Ho	Er	Tm	Yb	Lu	Hf	Ta	Pb	Th	U
Basalt Host																																
dc_1	ol	285	6.68	13.35	39.54	107	62.73	1047	13.6	66.0	5.60	1.73	572	28.2	54.0	6.37	25.34	4.47	1.22	4.16	0.52	3.01	0.59	1.33	0.22	1.68	0.14	1.61	0.22	9.46	6.13	2.08
dc_4	ol	144	260	406	7.62	79.49	31.77	516	7.20	28.86	2.26	0.68	243	12.3	23.08	2.67	12.65	2.53	0.74	1.89	0.24	1.73	0.39	0.80	0.08	0.82	0.08	0.72	0.10	3.74	2.70	0.85
dc_7	ol	234	501	32.97	31.29	54.66	35.58	950	9.91	55.6	3.11	0.91	355	19.1	38.5	4.51	20.04	3.70	1.00	3.03	0.39	2.29	0.29	1.18	0.12	0.79	0.13	1.35	0.17	3.50	2.64	0.94
dc_10	ol	214	17.93	2.70	132	104	45.01	1417	7.22	21.43	2.97	0.46	442	21.3	39.9	4.27	16.53	2.55	0.65	1.62	0.24	1.64	0.27	0.99	0.10	0.77	0.08	0.74	0.13	9.16	3.50	1.55
dc_12	ol	109	359	518	16.49	97.63	17.35	294	4.17	18.23	1.31	0.76	141	9.2	20.5	1.99	8.17	2.07	0.58	1.19	0.20	1.32	0.18	0.60	0.10	0.33	0.11	0.66	0.03	0.49	1.49	0.69
dc_13	ol	269	346	bdl	33.11	91.63	115	705	12.7	52.3	3.91	19.11	973	20.2	37.6	4.78	20.81	4.50	1.32	3.44	0.45	2.53	0.46	1.18	0.17	0.91	0.16	1.47	0.18	1.73	4.55	0.78
dc_14	ol	297	15.68	23.68	18.57	111	63	1152	14.8	67.7	5.77	1.68	586	30.7	57.6	6.48	27.87	5.67	1.55	3.70	0.53	3.04	0.59	1.48	0.25	1.18	0.24	1.75	0.26	9.43	6.52	2.09
dc_17	ol	259	378	25.72	135	162	29	860	12.5	44.2	3.59	1.29	331	19.9	36.4	4.32	17.58	3.91	1.25	3.19	0.49	2.51	0.48	1.16	0.16	1.17	0.16	1.21	0.18	6.47	3.79	1.43
Shoshonite Host																																
ea_1	cpx	130	1.06	4.21	177	108	209	692	25.3	186	23.2	9.28	878	77	135	14.05	51.5	9.04	1.69	5.87	0.88	4.85	0.91	2.56	0.39	2.48	0.39	4.93	1.23	26.59	32.48	10.10
ea_2	cpx	224	29.85	27.06	89.20	86.8	101	441	27.9	139	11.7	4.55	451	45	90	10.97	46.4	9.67	2.23	7.63	1.08	5.73	1.07	2.64	0.40	2.90	0.39	4.51	0.61	13.20	15.34	5.11
ea_3	cpx	114	bdl	1.91	210	110	234	769	23.9	203	25.4	10.46	952	78	138	13.82	48.9	7.78	1.65	5.44	0.84	4.40	0.86	2.22	0.39	2.69	0.39	5.37	1.34	29.13	35.16	11.36
ea_4	cpx	195	156	48.68	41.57	62.0	45	328	20.2	78	4.79	1.87	242	24.2	54	7.01	32.88	8.36	1.84	6.08	0.77	4.67	0.78	1.92	0.24	1.67	0.26	2.86	0.26	5.55	5.49	1.75
ea_5	cpx	124	238	28.92	83.55	65.5	117	493	13.6	87	11.9	5.03	574	35.0	63	6.94	27.03	5.51	1.39	4.36	0.57	3.04	0.57	1.01	0.21	1.40	0.22	2.73	0.69	15.26	15.56	5.56
ea_6	cpx	146	5.25	1.77	158	107	223	965	19.8	179	24.3	9.24	1166	75	129	12.61	45.1	7.65	1.75	5.03	0.70	3.93	0.80	2.11	0.28	2.00	0.30	4.55	1.24	28.98	30.41	9.64
ea_7	cpx	153	3.13	6.32	143	105	198	900	20.5	164	22.0	8.27	1046	68	119	12.18	45.2	8.08	1.70	5.24	0.76	4.00	0.74	2.02	0.30	2.08	0.29	4.11	1.12	26.03	27.67	8.76
ea_8	cpx	118	2.71	1.51	189	101	222	959	16.8	160	22.6	9.17	1137	67	115	11.42	39.93	6.96	1.48	4.67	0.61	3.26	0.64	1.57	0.24	1.72	0.25	3.85	1.07	28.52	27.81	8.79
ea_9	cpx	127	3.49	3.29	144	109	202	1054	18.3	156	20.8	7.63	1212	65	112	11.05	41.1	6.76	1.73	4.59	0.65	3.51	0.64	1.76	0.24	1.91	0.29	3.56	1.02	25.36	26.53	8.39
ea_10	cpx	208	70.43	17.65	127	132	160	668	26.3	164	19.6	6.30	828	75	137	14.77	58.3	10.35	2.23	7.60	1.03	5.25	1.00	2.30	0.37	2.51	0.36	4.55	0.97	21.10	24.27	7.59
ea_11	cpx	173	7.70	9.76	186	102	178	1284	17.0	141	17.9	7.37	1056	60	105	10.72	39.71	6.85	1.63	4.55	0.63	3.43	0.62	1.55	0.25	1.73	0.24	3.52	0.93	23.98	23.36	7.29
ea_12	cpx	127	1.67	1.22	203	105	206	839	18.4	180	23.9	7.84	1151	69	118	11.57	41.6	6.97	1.67	4.84	0.66	3.51	0.63	1.77	0.27	1.79	0.28	4.18	1.17	28.89	28.53	9.27
ea_13	cpx	117	3.92	0.99	195	100	227	779	17.9	181	24.6	8.97	1146	67	114	11.09	39.6	6.73	1.54	4.76	0.63	3.53	0.65	1.68	0.24	1.82	0.27	4.36	1.20	29.27	30.03	9.52
ea_14	cpx	156	15.17	5.94	65	92	160	1041	16.6	126	16.6	6.67	939	55	95	9.53	35.69	6.38	1.30	4.51	0.58	3.03	0.64	1.52	0.22	1.44	0.21	3.09	0.82	23.71	20.24	6.88
ea_15	cpx	169	24.12	26.69	132	107	112	557	26.0	123	12.1	4.79	520	55	103	11.64	48.0	9.78	1.98	7.16	0.95	5.31	1.05	2.48	0.38	2.39	0.34	3.77	0.62	13.59	17.28	5.12
ea_16	cpx	180	18.33	21.67	110	89	124	577	25.1	130	13.9	5.43	658	48	95	11.08	44.4	9.30	1.95	6.52	0.95	5.12	0.99	2.56	0.34	2.36	0.36	3.79	0.70	16.60	17.30	5.54
Latite Host																																
dd_2	cpx	118	bdl	7.39	249	101	219	845	19.3	175	24.6	9.63	1161	72	124	12.43	44.3	7.02	1.59	4.85	0.69	3.70	0.78	1.63	0.33	1.80	0.33	4.53	1.20	29.06	31.71	10.09
dd_3	cpx	115	42.8	3.31	160	82	206	619	19.7	170	21.2	8.75	838	62	108	10.91	40.3	7.69	1.62	4.92	0.70	4.05	0.68	2.01	0.35	1.88	0.28	4.69	1.13	24.75	29.43	9.08
dd_4	cpx	96	4.10	3.65	207	104	237	735	20.0	179	24.5	10.04	1090	72	122	12.19	42.9	7.43	1.56	4.78	0.65	3.88	0.75	2.10	0.28	2.42	0.32	4.82	1.27	29.56	34.61	11.24
dd_5	cpx	196	65.7	24.84	101	84	105	568	23.7	125	12.0	4.49	568	45	89	10.33	43.9	8.97	1.87	7.18	0.86	5.01	1.04	2.16	0.35	2.10	0.32	3.38	0.65	14.62	14.78	4.83
dd_6	cpx	190	3.96	16.25	245	98	159	660	24.5	165	17.7	6.67	801	59	109	11.77	47.8	8.68	2.19	6.77	0.94	4.86	0.94	2.76	0.33	2.45	0.32	4.49	0.92	21.50	22.83	6.87
dd_7	cpx	120	64.9	bdl	185	97	222	831	17.7	178	23.5	8.32	1109	66	109	11.08	40.5	7.24	1.67	4.53	0.75	3.71	0.84	1.78	0.25	1.95	0.30	4.13	1.13	27.60	27.50	8.82
dd_17	ol	98	10.12	116	151	231	152	651	14.8	130	16.5	6.29	839	54	94	9.43	31.85	5.56	0.91	3.46	0.47	2.73	0.48	0.93	0.16	1.36	0.26	3.07	0.87	35.44	21.84	6.77
dd_20	cpx	90	29.12	3.28	181	97	234	936	13.9	162	24.1	9.58	1295	67	107	9.96	34.5	5.06	1.23	3.65	0.53	2.80	0.50	1.39	0.23	1.23	0.21	3.70	1.26	33.52	31.52	10.03
dd_21	cpx	81	bdl	12.43	96	98	239	950	14.8	167	25.3	9.31	1245	71	114	10.64	35.6	5.57	1.38	3.52	0.42	2.12	0.49	1.56	0.19	1.28	0.24	3.45	1.20	32.72	32.13	9.99
dd_22	cpx	149	74.5	24.06	78	75	158	573	17.3	138	16.1	6.72	719	46	81	8.57	33.4	6.06	1.34	4.64	0.61	3.68	0.62	1.78	0.24	2.03	0.23	3.83	0.84	17.61	21.34	6.40
dd_23	cpx	113	21.55	1.49	231	107	250	788	18.8	185	25.2	10.24	1157	76	129	12.16	44.7	7.29	1.41	4.73	0.63	3.71	0.74	2.28	0.29	2.20	0.24	4.76	1.33	31.48	33.09	10.52

t4.46	*Trachyte Host*																														
t4.47	dd_10	cpx	107	bdl	bdl	215	105	244	1040	18.8	197	25.5	9.86	1279	80	138	13.20	48.1	8.14	1.78	3.99	0.65	3.57	0.70	1.95	0.31	2.16	0.28	4.94	1.31	32.20	33.63	10.59
t4.48	dd_11	cpx	102	41.0	bdl	201	112	246	1037	18.1	201	28.5	9.73	1326	84	141	13.99	48.8	7.81	1.47	4.87	0.66	3.42	0.58	1.70	0.24	1.94	0.27	4.81	1.48	33.42	34.86	10.47
t4.49	dd_16	ol	164	39.0	bdl	109	66	252	742	18.3	221	29.2	10.80	805	75	125	11.71	42.3	7.44	1.16	4.31	0.60	3.58	0.64	1.41	0.33	1.72	0.31	5.30	1.37	36.53	37.21	11.75
t4.50	cb_3	ol	80.0	7.36	8.51	20.1	90	247	835	19.9	200	27.7	12.70	1963	63	109	10.23	35.4	8.14	0.75	5.28	0.85	2.63	0.54	2.13	0.35	3.34	0.03	4.66	1.31	34.88	30.17	11.41
t4.51	cb_4	ol	59.8	bdl	18.65	23.5	169	198	760	15.0	137	18.8	7.77	1894	48	83	8.94	30.01	6.73	2.29	7.72	0.33	1.83	0.67	1.56	bdl	1.41	0.05	3.37	1.11	24.80	20.51	6.43
t4.52	cb_6	cpx	34.1	79.4	bdl	8.9	49	212	451	17.8	194	20.8	7.79	866	45	87	7.76	29.85	5.86	0.95	6.90	0.69	3.77	0.38	2.80	0.50	1.81	0.27	2.97	1.22	24.12	26.13	7.95
t4.53	da_1	cpx	45.0	14.26	bdl	16.8	70	257	712	16.4	180	22.3	10.29	1578	57	99	8.67	30.85	4.11	1.27	4.26	0.33	3.28	0.59	1.41	0.17	0.84	0.21	3.95	1.18	26.94	28.45	9.71
t4.54	da_2	cpx	77.3	8.99	7.97	64	91	246	936	16.5	169	23.6	10.44	1699	67	112	10.76	34.7	6.75	1.34	2.11	0.54	4.52	0.54	1.99	0.23	2.64	0.26	3.48	1.46	45.2	29.83	10.90
t4.55	da_3	cpx	66.7	10.44	bdl	32.7	109	226	887	23.8	157	19.5	9.02	1769	64	118	12.21	43.4	8.11	1.60	7.34	0.49	4.30	1.34	2.22	0.47	1.38	0.30	4.76	1.03	24.52	25.79	8.86
t4.56	da_4	cpx	44.2	bdl	bdl	13.3	86	216	695	16.2	183	20.3	9.07	1561	63	106	10.27	39.2	5.49	1.56	6.54	0.39	3.75	0.57	1.39	0.35	2.34	0.30	3.96	1.37	26.43	28.45	9.69
t4.57	da_5	cpx	63.8	42.0	bdl	17.5	82	229	856	16.3	179	20.7	9.40	1880	55	90	8.86	31.76	6.86	1.23	3.72	0.36	3.08	0.43	0.81	0.32	2.31	0.37	6.27	1.02	24.58	28.10	8.42
t4.58	da_6	cpx	58.5	36.9	bdl	23.2	85	208	767	22.3	194	18.0	7.84	1658	57	105	10.49	37.83	6.94	1.63	5.14	0.79	4.69	0.77	3.01	0.40	2.67	0.33	4.68	1.06	23.05	23.61	7.86
t4.59	da_7	cpx	45.0	33.14	bdl	21.7	88	234	669	25.4	177	22.1	9.91	1273	83	140	14.41	48.7	7.41	1.55	5.70	0.66	5.04	0.83	2.86	0.45	2.89	0.38	4.03	1.07	28.73	35.79	10.36
t4.60																																	
t4.61	*Rhyolite Host*																																
t4.62	ca_1	sa	1.79	bdl	bdl	27.6	nd	454	5.46	37.5	228	38.4	24.17	1.39	131	208	19.46	66.0	9.36	0.26	5.79	1.43	6.94	1.51	3.76	0.63	3.87	0.68	8.10	2.76	46.3	76.1	21.99
t4.63	ca_2	sa	1.87	16.31	9.98	67	nd	373	9.21	31.3	182	29.6	17.81	2.21	105	169	15.26	49.8	8.31	0.32	5.49	1.00	5.30	1.05	2.92	0.47	3.40	0.47	6.32	1.77	36.18	58.2	17.64
t4.64	ca_3	sa	1.22	bdl	20.24	52	nd	298	6.93	25.3	151	24.6	15.90	bdl	85	140	13.34	42.2	6.16	0.09	5.22	0.72	4.24	0.92	2.16	0.43	3.11	0.38	5.61	1.64	29.68	52.6	14.88
t4.65	ca_5	sa	0.84	bdl	bdl	44	nd	346	7.79	26.0	168	26.6	16.92	2.53	98	158	13.86	46.6	7.92	0.14	3.87	0.64	4.23	0.82	2.91	0.42	2.93	0.46	5.95	1.88	35.44	56.3	18.17
t4.66	ca_6	sa	bdl	bdl	bdl	40	nd	353	25.8	33.4	312	32.4	17.69	7.81	111	203	19.41	68.1	9.41	0.52	6.98	0.96	6.98	1.13	4.21	0.35	6.20	0.86	10.71	2.08	34.86	71.2	18.98
t4.67	ca_7	sa	0.73	13.78	bdl	38	nd	342	21.3	31.8	303	30.8	14.05	7.61	103	168	16.15	53.1	9.21	0.52	3.52	1.11	5.79	1.14	2.74	0.52	4.08	0.65	10.16	2.06	36.12	58.3	16.11
t4.68	ca_9	sa	2.10	bdl	bdl	43	nd	327	21.4	26.7	413	28.8	15.93	8.38	90	154	14.27	50.0	5.00	0.59	5.51	0.73	4.34	1.11	3.18	0.57	3.61	0.54	10.32	1.74	31.37	49.4	15.77
t4.69	ca_12	sa	0.63	bdl	11.60	53	nd	310	17.9	31.0	368	28.6	15.63	3.79	106	173	16.81	56.1	9.11	0.28	6.27	0.91	5.62	1.13	2.46	0.43	3.44	0.56	9.06	1.75	32.94	53.4	16.78
t4.70	ca_13	sa	1.79	bdl	bdl	57	nd	354	16.3	32.7	402	30.3	17.23	2.60	111	180	17.48	57.2	8.28	0.26	7.18	0.98	5.08	1.07	3.57	0.46	3.51	0.72	10.56	1.92	34.27	58.6	17.28
t4.71	ca_14	sa	1.37	bdl	bdl	41	nd	308	28.3	28.5	283	31.9	14.98	8.86	94	158	14.46	46.6	8.41	0.33	4.70	0.82	5.21	1.06	2.76	0.43	3.18	0.62	7.65	1.88	33.16	53.6	15.62
t4.72	ca_16	sa	0.65	bdl	bdl	41	nd	330	11.3	26.5	344	27.6	14.45	1.90	87	142	13.27	43.8	7.24	0.39	5.16	0.71	4.67	1.18	3.44	0.44	3.48	0.45	8.71	1.72	31.80	48.1	14.17
t4.73	ca_17	sa	bdl	bdl	bdl	54	nd	344	6.7	25.0	207	26.2	15.15	3.74	85	143	13.70	46.7	7.24	0.27	4.73	0.74	4.62	0.96	2.86	0.30	2.74	0.51	6.59	1.32	30.45	46.7	15.07
t4.74	ca_18	sa	bdl	bdl	bdl	60	nd	361	13.2	27.5	199	29.3	19.27	3.48	105	171	16.13	51.2	8.02	0.24	5.05	0.80	5.20	1.17	2.93	0.46	2.86	0.52	7.38	2.02	35.73	61.1	18.53
t4.75	ca_19	sa	bdl	bdl	bdl	44	nd	328	20.1	26.9	222	29.2	18.29	8.50	96	155	14.20	46.0	7.54	0.20	4.67	0.75	4.96	0.96	2.94	0.36	2.77	0.54	6.43	2.28	37.42	62.2	18.97
t4.76	ca_20	sa	0.96	bdl	bdl	44	nd	296	21.3	24.5	191	26.1	16.26	8.65	88	141	13.50	43.6	7.44	0.43	3.40	0.88	3.96	0.96	2.53	0.52	2.42	0.43	5.92	1.77	30.45	52.7	16.89

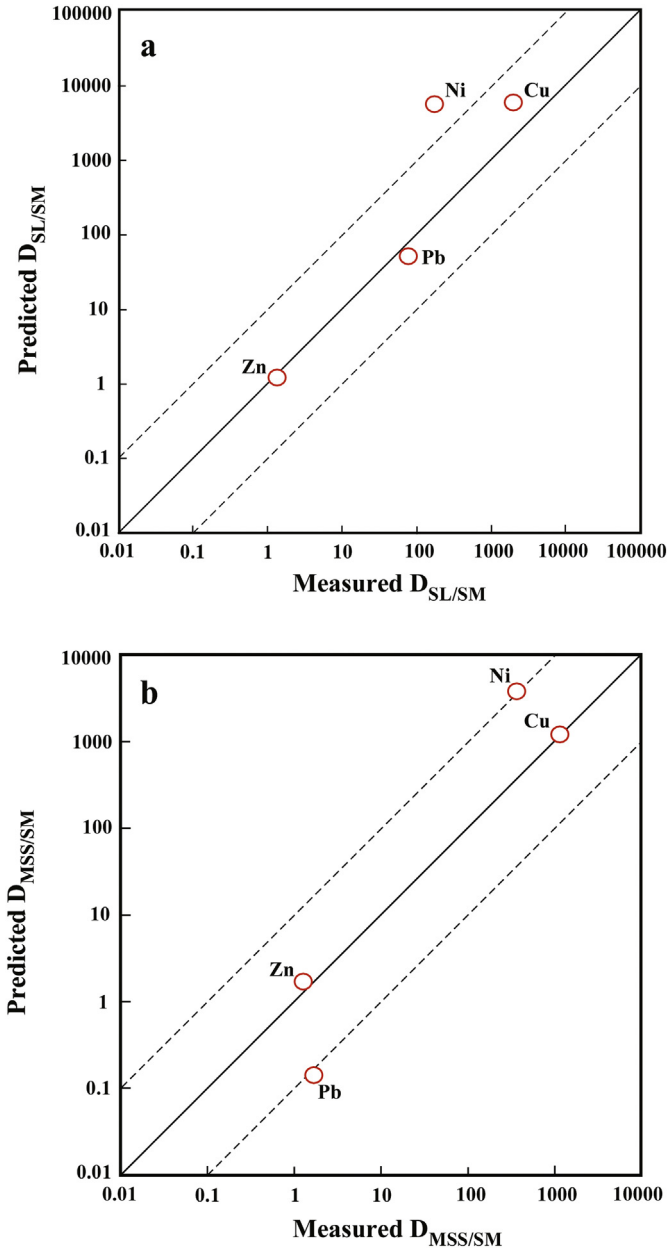

Fig. 4. Comparison of measured sulfide - silicate melt partition coefficients with values predicted by the model of Li and Audétat (2015); (a) sulfide liquid (Type 1 SIs)-silicate melt (b) monosulfide solid solution (Type 2 SIs)-silicate melt. T of 950 °C, ΔFMQ = −0.77 and FeO in the melt = 4.4 wt% estimated for La Fossa trachyte by Fulignati et al. (2018) have been used in the model.

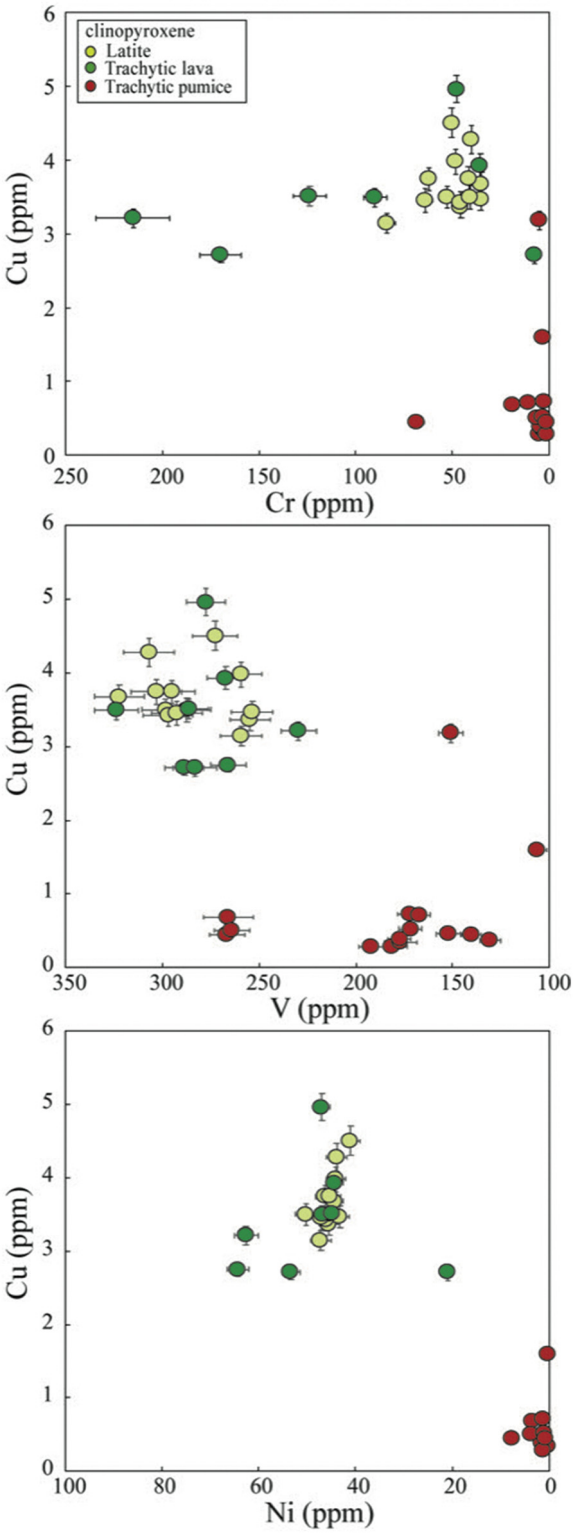

Fig. 5. Cu versus Cr, V and Ni content for clinopyroxene crystals in the latitic and trachytic products of La Fossa hosting the type 1 (yellow and green symbols) and type 2 (red symbols) SIs. See the supplementary material S1 for the complete data set of analyses of clinopyroxene. 1 sigma error for each analysis is shown as error bars, which if not visible, is smaller than the symbol. (For interpretation of the references to colour in this figure legend, the reader is referred to the web version of this article.)

event occurred at La Fossa volcano during XIII Cent. AD. This eruption produced a high amount of lithics which showed acid-sulfate alteration (Gurioli et al., 2012). Interestingly, S/Cu, Zn/Cu, Pb/Cu ratios measured on the fine ash of the Breccia di Commenda deposits are higher than the same ratios measured in the trachytic and rhyolitic SIs (Fig. 6a). This suggests that Cl-rich fluids carrying Pb and Zn from the magmatic-hydrothermal system were involved in the Breccia di Commenda eruption.

5.3. Comparison with mineralized systems

With the aim to compare the SIs composition in the products of an active arc volcano with that of SIs from magmas associated with porphyry mineralization, absolute and Cu-normalized metal concentrations from La Fossa are compared with those found in well-preserved SIs of ore-related igneous rocks. The metal ratios and absolute concentrations in Vulcano SIs (either in Type 1 and Type 2

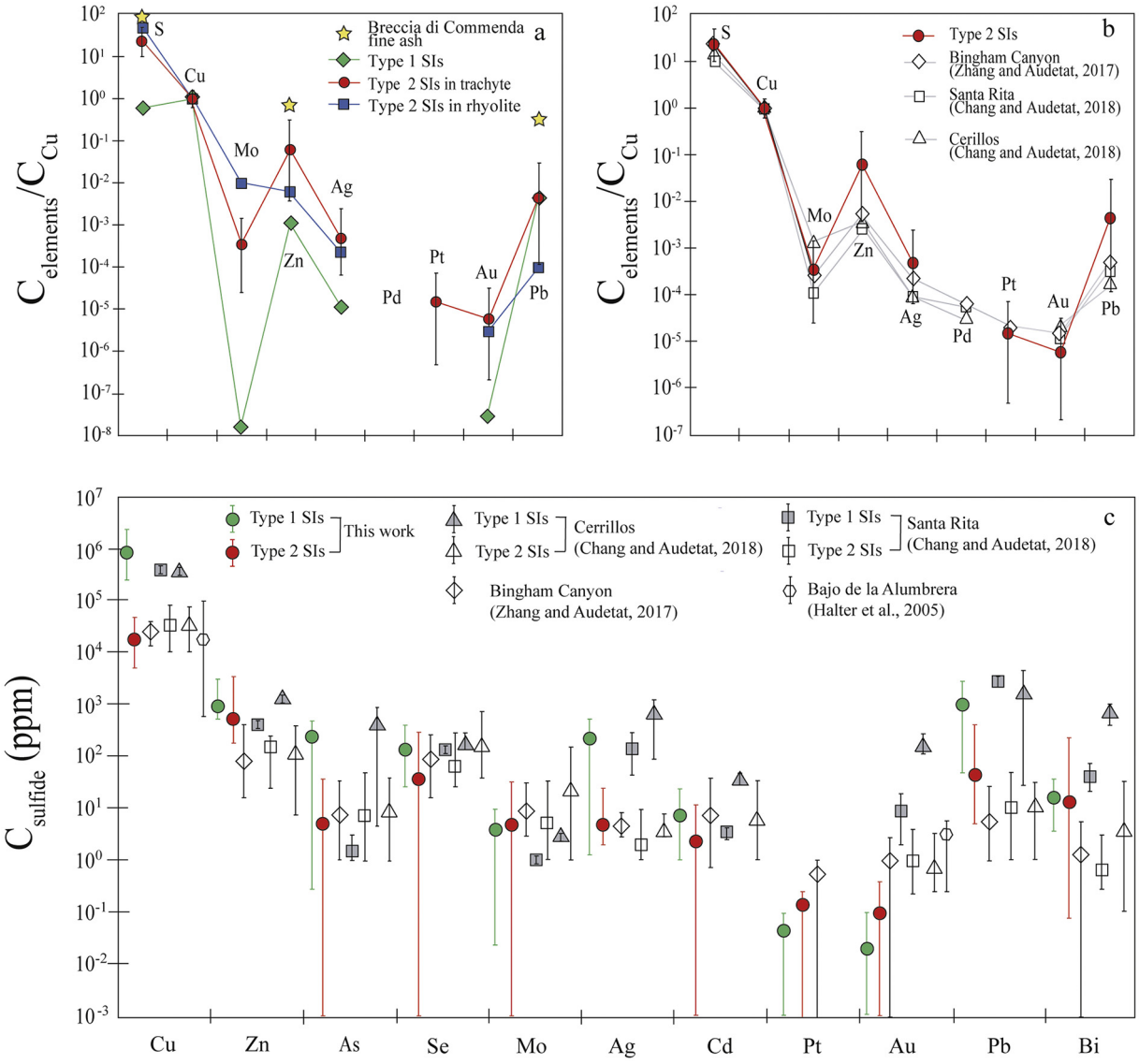

Fig. 6. (a) Cu-normalized composition of La Fossa SIs and Breccia di Commenda fine ash; (b) Cu-normalized composition (average and range) of Type 2 SIs compared to SIs of ore-related latitic magma at Bingham and at Santa Rita and Cerrillos; (c) Absolute metal concentrations in Type 1 and Type 2 La Fossa SIs compared with those found in mineralized systems (Bingham Canyon, Santa Rita, Cerrillos and Bajo de la Alumbrera).

SIs) match well with those of mineralized systems (Fig. 6b, c). This suggests that, at Vulcano, the late attainment of sulfide saturation during fractionation in mid-upper crustal reservoirs prevents the early depletion in S and chalcophile metals and produces magmatic sulfide melts with compositions comparable to those found in several porphyry systems. Once formed, the sulfides may be stored in crystal mushes of intermediate to evolved crustal reservoirs, re-melted by mafic sulfide-undersaturated recharges or eventually cannibalized by aqueous fluids exsolving at the rhyolite stage, thereby producing highly mineralizing solutions (Audétat and Simon, 2012; Halter et al., 2002; Keith et al., 1997; Nadeau et al., 2010; Wilkinson, 2013).

Our results indicate that the processes governing metal evolution through silicate melt differentiation in active arc magmatic systems share similarities to those inferred for magmas associated to porphyry Cu systems. Bearing in mind that the magmatic stage is arguably pivotal in the evolution of porphyry Cu systems (Audétat and Simon, 2012), arc volcanoes such as La Fossa can thus be viewed as active analogues and ideal sites for studying the critical early stages of porphyry Cu genesis. Their possibility to evolve toward mineralized systems will, of course, depend also on other factors (magma chamber size and depth, duration of magmatic and hydrothermal activity, and the efficiency of magmatic fluid focusing; Richards, 2011; Wilkinson, 2013) that can either promote or inhibit porphyry Cu formation.

6. Conclusive remarks

In this work, we used combined compositional data (major, minor and trace element) on melt inclusions, magmatic sulfides and host minerals from the eruptive products of the arc volcano of La Fossa (Vulcano Island, Italy), to track the evolution of metals along the magma differentiation path of an active magmatic system. We found that, in case of sulfide-undersaturated, volatile-rich arc basalts, metals are scarcely subtracted by degassing during ascent to shallow crustal reservoirs and thus reach their highest abundances in intermediate magmas. Further evolution results in sulfide saturation where Cu and chalcophile metals strongly partition into the sulfide melt, causing a dramatic decrease in abundance from the silicate melt. The evolution of Cu in the silicate melts was modeled with quantitative fractional crystallization, and

the results are in close agreement with experimental data. The model shows that fractionation of only 0.2–0.3 wt% of sulfide is sufficient to deplete the silicate melt in Cu down to the values recorded by MIs in trachytic and rhyolitic products. Metals that do not partition in sulfides (Pb, Zn) increase their concentrations with magmatic evolution until they are scavenged by a Cl-rich aqueous fluid phase, possibly exsolved at the rhyolitic stage.

The comparison of metal ratios and absolute concentrations of the Vulcano magmatic sulfides with those of sulfides found in magmatic rocks, associated with world-class porphyry Cu systems, shows strong similarities. This suggests that the processes governing metal evolution through silicate melt differentiation in active arc magmatic systems are similar to those processes inferred for magmatic stage of porphyry Cu environments. Our results thus suggest that the investigation of metal evolution in active arc volcanoes such as La Fossa can provide information for interpreting the genetic mechanisms of porphyry Cu deposit formation.

Declaration of Competing Interest

The authors declare that they have no known competing financial interests or personal relationships that could have appeared to influence the work reported in this paper.

Acknowledgements

We warmly thank Prof. Jung-Woo Park for the review of an early version of the manuscript. We would also like to thank Greg Shellnutt for editorial handling. The present manuscript benefited from the constructive review of two anonymous referees whose comments and suggestions helped to improve the quality and clarity of the manuscript. The authors thank R. Ishak (Università di Pisa), A. Risplendente (Università di Milano), for assistance during analytical work, F. Colarieti and M. Gemelli (Università di Pisa) for sample preparation and M. D. Suttle for helping us with English editing. This research was funded by projects PRA_2018_41 to PF and MP and FFABR2017 to AG. This research is part of SC PhD program funded by a Tuscany Regional "Pegaso" doctoral grant.

Appendix A. Supplementary data

References

Audétat, A., Simon, A.C., 2012. Magmatic controls on porphyry copper genesis. In: Hedenquist, J.W., et al. (Eds.), Geology and Genesis of Major Copper Deposits and Districts of the World: A Tribute to Richard H. Sillitoe. 16. Society of Economic Geologists Special Publications, pp. 1–18.

Bai, Z.-J., Zhong, H., Hu, R.-Z., Zhu, W.-G., 2020. Early sulfide saturation in arc volcanic rocks of Southeast China: Implications for the formation of co-magmatic porphyry–epithermal Cu–Au deposits. Geochim. Cosmochim. Acta 280, 66–84.

Boyce, A.J., Fulignati, P., Sbrana, A., Fallick, A.E., 2007. Fluids in early stage hydrothermal alteration of high-sulfidation epithermal systems: a view from the Vulcano active hydrothermal system (Aeolian Island, Italy). J. Volcanol. Geotherm. Res. 166, 76–90.

Candela, P.A., Holland, H.D., 1984. The partitioning of copper and molybdenum between silicate melts and aqueous fluids. Geochim. Cosmochim. Acta 48, 373–380.

Chang, J., Audétat, A., 2018. Petrogenesis and metal content of Horneblende-rich Xenoliths from two Laramide-age Magma systems in Southwestern USA: insights into the Metal Budget of Arc Magmas. J. Petrol. 59, 1869–1898.

Chen, K., Tang, M., Lee, C.-T.A., Wang, Z., Zou, Z., Hu, Z., Liu, Y., 2020. Sulfide-bearing cumulates in deep continental arcs: the missing copper reservoir. Earth Planet. Sci. Lett. 531, 115971. https://doi.org/10.1016/j.epsl.2019.115971.

Costa, S., Masotta, M., Gioncada, A., Pistolesi, M., Bosch, D., Scarlato, P., 2020. Magma evolution at La Fossa volcano (Vulcano Island, Italy) in the last 1000 years: evidence from eruptive products and temperature gradient experiments. Contrib. Mineral. Petrol. 175, 31.

Cox, D., Watt, S.F.L., Jenner, F.E., Hastie, A.R., Hammond, S.J., 2019. Chalcophile element processing beneath a continental arc stratovolcano. Earth Planet. Sci. Lett. 522, 1–11.

Craig, J.R., Kullerud, G., 1969. Phase relations in the Cu-Fe-Ni-S system and their application to magmatic ore deposits. Econ. Geol. Monogr. 4, 344–358.

De Astis, G., Peccerillo, A., Kempton, P.D., La Volpe, L., Wu, T.W., 2000. Transition from calc-alkaline to potassium-rich magmatism in subduction environments: geochemical and Sr, Nd, Pbisotopic constraints from the island of Vulcano (Aeolian arc). Contrib. Mineral. Petrol. 139, 684–703.

De Astis, G., Lucchi, F., Dellino, P., La Volpe, L., Tranne, C.A., Frezzotti, M.L., Peccerillo, A., 2013. Geology volcanic history and petrology of Vulcano (central Aeolian archipelago). Geol. Soc. Lond. Mem. 37, 281–349.

Fulignati, P., Gioncada, A., Sbrana, A., 1998. Geologic model of the magmatic-hydrothermal system of Vulcano (Aeolian Island, Italy). Mineral. Petrol. 62, 195–222.

Di Traglia, F., Pistolesi, M., Rosi, M., Bonadonna, C., Fusillo, R., Roverato, M., 2013. Growth and erosion: The volcanic geology and morphological evolution of La Fossa (Island of Vulcano, Southern Italy) in the last 1000 years. Geomorphology 194, 94–107. https://doi.org/10.1016/j.geomorph.2013.04.018.

Fulignati, P., Gioncada, A., Costa, S., Di Genova, D., Di Traglia, F., Pistolesi, M., 2018. Magmatic sulfide immiscibility at an active magmatic-hydrothermal system: the case of la Fossa (Vulcano, Italy). J. Volcanol. Geotherm. Res. 358, 45–57.

Fusillo, R., Di Traglia, F., Gioncada, A., Pistolesi, M., Wallace, P.J., Rosi, M., 2015. Deciphering post-caldera volcanism: insight into the Vulcanello (Island of Vulcano, Southern Italy) eruptive activity based on geological and petrological constraints. Bull. Volcanol. 77, 76.

Georgatou, A., Chiaradia, M., 2020. Magmatic sulfides in high-potassium calc-alkaline to shoshonitic and alkaline rocks. Solid Earth 11, 1–21.

Georgatou, A., Chiaradia, M., Rezeau, H., Walle, M., 2018. Magmatic sulphides in Quaternary Ecuadorian arc magmas. Lithos 296-299, 580–599.

Gioncada, A., Clocchiatti, R., Sbrana, A., Bottazzi, P., Massare, D., Ottolini, L., 1998. A study of melt inclusions at Vulcano (Aeolian Islands, Italy): insights on the primitive magmas and on the volcanic feeding system. Bull. Volcanol. 60, 286–306.

Gurioli, L., Zanella, E., Gioncada, A., Sbrana, A., 2012. The historic magmatic-hydrothermal eruption of the Breccia di Commenda, Vulcano, Italy. Bull. Volcanol. 74, 1235–1254.

Halter, W.E., Pettke, T., Heinrich, C.A., 2002. The origin of Cu/au ratios in porphyry-type ore deposits. Science 296, 1844–1846.

Halter, W.E., Heinrich, C.A., Pettke, T., 2005. Magma evolution and the formation of porphyry Cu-Au ore fluids: evidence from silicate and sulfide melt inclusions. Mineral. Deposita 39, 845–863.

Hao, H., Campbell, I.H., Richards, J.P., Nakamura, E., Sakaguchi, C., 2019. Platinum-group element geochemistry of the Escondida Igneous suites, Northern Chile: Implications for ore formation. J. Petrol. 60, 487–524.

Hedenquist, J.W., Lowenstern, J.B., 1994. The role of magmas in the formation of hydrothermal ore-deposits. Nature 370, 519–527.

Jenner, F.E., O'Neill, H.S.C., Arculus, R.J., Mavrogenes, J.A., 2010. The magnetite crisis in the evolution of arc-related magmas and the initial concentration of Au, Ag and Cu. J. Petrol. 51, 2445–2464.

Keith, J.D., Whitney, J.A., Hattori, K., Ballantyne, G.H., Christiansen, E.H., Barr, D.L., Cannan, T.M., Hook, C.J., 1997. The role of magmatic sulfides and mafic alkaline magmas in the Bingham and Tintic mining districts, Utah. J. Petrol. 38, 1679–1690.

Le Voyer, M., Asimow, P.D., Mosenfelder, J.L., Guan, Y., Wallace, P.J., Schiano, P., Stolper, E.M., Eiler, J.M., 2014. Zonation of H_2O and F concentrations around melt inclusions in olivines. J. Petrol. 55, 685–707.

Li, Y., Audétat, A., 2015. Effects of temperature, silicate melt composition, and oxygen fugacity on the partitioning of V, Mn, Co, Ni, Cu, Zn, As, Mo, Ag, Sn, Sb, W, Au, Pb, and Bi between sulfide phases and silicate melt. Geochim. Cosmochim. Acta 162, 25–45.

Mungall, J.E., Brenan, J.M., Godel, B., Barnes, S.J., Gaillard, F., 2015. Transport of metals and Sulphur in magmas by flotation of sulphide melt on vapour bubbles. Nat. Geosci. 8, 216–219.

Nadeau, O., Williams-Jones, A.E., Stix, J., 2010. Sulphide magma as a source of metals in arc-related magmatic hydrothermal ore fluids. Nat. Geosci. 3, 501–505.

Paonita, A., Federico, C., Bonfanti, P., Capasso, G., Inguaggiato, S., Italiano, F., Madonia, P., Pecoraino, G., Sortino, F., 2013. The episodic and abrupt geochemical changes at La Fossa fumaroles (Vulcano Island, Italy) and related constraints on the dynamics, structure, and compositions of the magmatic system. Geochim. Cosmochim. Acta 120, 158–178.

Parat, F., Holtz, F., Streck, M.J., 2011. Sulfur-bearing magmatic accessory minerals. Rev. Mineral. Geochem. 73, 285–314.

Park, J.-W., Campbell, I.H., Arculus, R.J., 2013. Platinum-alloy and sulfur saturation in an arc-related basalt to rhyolite suite: evidence from the Pual Ridge lavas, the Eastern Manus Basin. Geochim. Cosmochim. Acta 101, 76–95.

Park, J.-W., Campbell, I.H., Kim, J., Moon, J.W., 2015. The role of late sulfide saturation in the formation of a Cu- and Au-rich Magma: Insights from the platinum group element geochemistry of Niuatahi-Motutahi Lavas, Tonga Rear Arc. J. Petrol. 56, 59–81.

Park, J.-W., Campbell, I.H., Malaviarachchi, S.P.K., Cocker, H., Hao, H., Kay, S.M., 2019. Chalcophile element fertility and the formation of porphyry Cu ± Au deposits. Mineral. Deposita 54, 657–670.

Peccerillo, A., Frezzotti, M.L., De Astis, G., Ventura, G., 2006. Modeling the magma plumbing system of Vulcano (Aeolian Islands, Italy) by integrated fluid-inclusion geobarometry, petrology, and geophysics. Geology 34, 17–20.

Richards, J.P., 2011. Magmatic to hydrothermal metal fluxes in convergent and collided margins. Ore Geol. Rev. 40, 1–26.

Richards, J.P., 2015. The oxidation state, and sulfur and Cu contents of arc magmas: implications for metallogeny. Lithos 233, 27–45.

Rosi, M., Di Traglia, F., Pistolesi, M., Esposti Ongaro, T., de Michieli Vitturi, M., Bonadonna, C., 2018. Dynamics of shallow hydrothermal eruptions: new insights from Vulcano's Breccia di Commenda eruption. Bull. Volcanol. 80, 8.

Rottier, B., Audétat, A., Kodera, P., Lexa, J., 2019. Origin and evolution of magmas in the porphyry Au -mineralized Javorie volcano (Central Slovakia): evidence from

thermodynamics, melt inclusions, and sulfide saturation. J. Petrol. 58 (12), 2449–2482. https://doi.org/10.1093/petrology/egaa014.
Scaillet, B., MacDonald, R., 2006. Experimental and thermodynamic constraints on the Sulphur yield of peralkaline and metaluminous silicic flood eruptions. J. Petrol. 47, 1413–1437.
Scaillet, B., Pichavant, M., 2005. A model of Sulphur solubility for hydrous mafic melts: application to the determination of magmatic fluid compositions of Italian volcanoes. Ann. Geophys. 48, 671–698.
Sillitoe, R.H., 2010. Porphyry copper systems. Econ. Geol. 105, 3–41.
Timm, C., de Ronde, C.E.J., Leybourne, M.I., Layton-Matthews, D., Graham, I.J., 2012. Sources of chalcophile and siderophile elements in kermadec arc lavas. Econ. Geol. 107, 1527–1538.
Wilkinson, J.J., 2013. Triggers for the formation of porphyry ore deposits in magmatic arcs. Nat. Geosci. 6, 917–925.
Zajacz, Z., Halter, W.E., Pettke, T., Guillong, M., 2008. Determination of fluid/melt partition coefficients by LA-ICPMS analysis of co-existing fluid and silicate melt inclusions: controls on element partitioning. Geochim. Cosmochim. Acta 72, 2169–2197.
Zajacz, Z., Candela, P.A., Piccoli, P.M., Sanchez-Valle, C., 2012. Gold and copper in volatile saturated mafic to intermediate magmas: solubilities, partitioning and implications or ore deposit formation. Geochim. Cosmochim. Acta 91, 140–159.
Zelenski, M., Kamenetsky, V.S., Mavrogenes, J.A., Gurenko, A.A., Danyushevsky, L.V., 2018. Silicate-sulfide liquid immiscibility in modern arc basalt (Tolbachik volcano, Kamchatka): part I. Occurrence and compositions of sulfide melts. Chem. Geol. 478, 102–111.
Zhang, D., Audétat, A., 2017. What caused the formation of the giant bingham canyon porphyry Cu-Mo-Au deposit? Insights from melt inclusions and magmatic sulfides. Econ. Geol. 112, 221–244.